Photoconductive Hybrid Films via Directional Self-Assembly of C_{60} on Aligned Carbon Nanotubes

*Eric R. Meshot, Keval D. Patel, Sameh Tawfick, K. Anne Juggernauth, Mostafa Bedewy, Eric A. Verploegen, Michaël F. L. De Volder, and A. John Hart**

Hybrid nanostructured materials can exhibit different properties than their constituent components, and can enable decoupled engineering of energy conversion and transport functions. Novel means of building hybrid assemblies of crystalline C_{60} and carbon nanotubes (CNTs) are presented, wherein aligned CNT films direct the crystallization and orientation of C_{60} rods from solution. In these hybrid films, the C_{60} rods are oriented parallel to the direction of the CNTs throughout the thickness of the film. High-resolution imaging shows that the crystals incorporate CNTs during growth, yet grazing-incidence X-ray diffraction (GIXD) shows that the crystal structure of the C_{60} rods is not perturbed by the CNTs. Growth kinetics of the C_{60} rods are enhanced 8-fold on CNTs compared to bare Si, emphasizing the importance of the aligned, porous morphology of the CNT films as well as the selective surface interactions between C_{60} and CNTs. Finally, it is shown how hybrid C_{60}–CNT films can be integrated electrically and employed as UV detectors with a high photoconductive gain and a responsivity of 10^5 A W^{-1} at low biases (± 0.5 V). The finding that CNTs can induce rapid, directional crystallization of molecules from solution may have broader implications to the science and applications of crystal growth, such as for inorganic nanocrystals, proteins, and synthetic polymers.

1. Introduction

Fullerenes (C_{60}) are a uniquely monodisperse nanoscale building block and can be assembled into nano- and microscale crystals with diverse and controllable sizes and shapes using evaporation of dispersions.[1–6] Crystalline C_{60} is a direct-band gap semiconductor,[7] an excellent electron acceptor,[7,8] and calculations show that contacts between C_{60} molecules in a closely packed crystal have very low thermal conductance.[9] These features make C_{60} attractive for applications including diodes,[8,10] field-effect transistors,[11] photoelectrics,[5,12] and thermoelectrics.[9] C_{60} crystals are generally made in bulk or deposited randomly on substrates; however, directed placement, alignment, and interconnection of C_{60} crystals is typically necessary for their utilization in devices, and this remains a challenge.

We demonstrate that aligned carbon nanotube (CNT) films can spatially direct the crystallization of C_{60} from solution, therefore enabling integration of hybrid thin-film devices by combining standard photolithography and two-step capillary self-assembly process. Uniquely, we find that C_{60} rods crystallize preferentially parallel to films of horizontally aligned CNTs, thus creating a self-organized directional assembly, wherein C_{60} crystals are pierced and interconnected by CNT conduits. We find that the kinetics of C_{60} crystallization are 8-fold faster on CNTs than on bare Si, but the dimensions of the rods are the same. The resultant hybrid film is advantageous for energy devices, especially considering that C_{60} crystals alone are poor electrical conductors. To this end, we demonstrate that the C_{60}–CNT hybrid films have high photoconductive gain under UV irradiation with a responsivity as high as 10^5 A W^{-1} at low biases (± 0.5 V). Overall, the rational design and fabrication of templates that induce ordered crystallization, and the understanding of how nanostructured surfaces affect crystallization kinetics, are important topics for applications including organic electronics,[13] composite materials, and protein science.[14,15]

2. Synthesis of C_{60}-CNTs Hybrid Films

Directed crystallization of C_{60} on CNTs is achieved, as shown in **Figure 1**. First, vertically aligned CNT "forests" are grown from lithographically patterned catalyst on silicon wafers using a standard catalytic chemical vapor deposition (CVD) process.[16,17] The forests comprise multi-walled CNTs with a mean diameter of 11 ± 2.8 nm.[18] Next, the vertical CNTs are

E. R. Meshot, K. D. Patel, S. Tawfick, K. A. Juggernauth, M. Bedewy, Prof. A. J. Hart
Department of Mechanical Engineering
University of Michigan
2350 Hayward Street, Ann Arbor, MI 48104, USA
E-mail: ajohnh@umich.edu
Dr. E. A. Verploegen
Stanford Synchrotron Radiation Lightsource
SLAC National Accelerator Laboratory
2575 Sand Hill Road, Menlo Park, CA 94025, USA
Dr. M. F. L. De Volder
IMEC, Kapeldreef 75
3001 Heverlee, Belgium
Department of Mechanical Engineering
KULeuven, Celestijnenlaan 300B, 3001 Leuven, Belgium

DOI: 10.1002/adfm.201102393

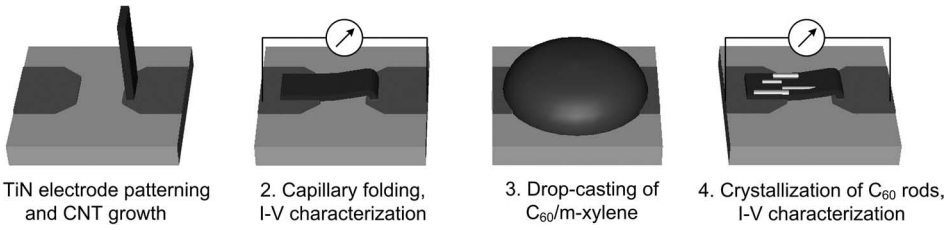

Figure 1. Fabrication of C_{60}-CNT hybrid films and device integration: a) process sequence involving CNT growth on patterned TiN electrodes and folding of vertical CNTs to produce horizontally oriented films, followed by wetting and drying with C_{60} dispersion in *m*-xylene. *I–V* characterization with and without UV exposure is performed before and after C_{60} crystallization.

transformed to a horizontal orientation via capillary folding by condensation of acetone onto the substrate.[19,20] Because the direction of capillary folding depends on the geometry of the CNT microstructures,[20] capillary folding enables fabrication of not only unidirectional films (**Figure 2**c) but also multidirectional CNT patterns, such as radially oriented (not shown) and adjacently perpendicular CNT films that overlap during capillary folding (Figure 2c). This method results in uniform-thickness CNT films with high packing fraction (≈0.2)[19] and high in-plane anisotropy. Further, the CNT films can be folded such that they bridge a set of prepatterned electrodes (in this case TiN). This provides a straight-forward and robust method for electrical integration of the C_{60}-CNT hybrids into sensors or other devices requiring electrical read-out. The in-plane anisotropy of the folded CNT sheets was previously quantified by X-ray scattering[19] and electrical resistance measurements. Finally, C_{60} dispersed in *m*-xylene (without surfactants)[1,4,6] is deposited by drop-casting onto the CNT films. The solution infiltrates the CNT film by capillary action and then is allowed to evaporate under ambient conditions. C_{60} rods crystallize on and within the CNT film during wetting and evaporation. Additional experimental details can be found in the Supporting Information.

3. Characterization of Alignment and Structure

We observe that the major axis (length) of each C_{60} rod is oriented along the direction of CNTs within the film, in both unidirectional and multidirectional sheets. This is shown in Figure 2b–c. In comparison, alignment is not observed in a control experiment where C_{60} crystallization is performed on the polished side of a bare (100) silicon wafer (Figure 2b). We quantify the average orientation of the C_{60} rods by the mean square cosine

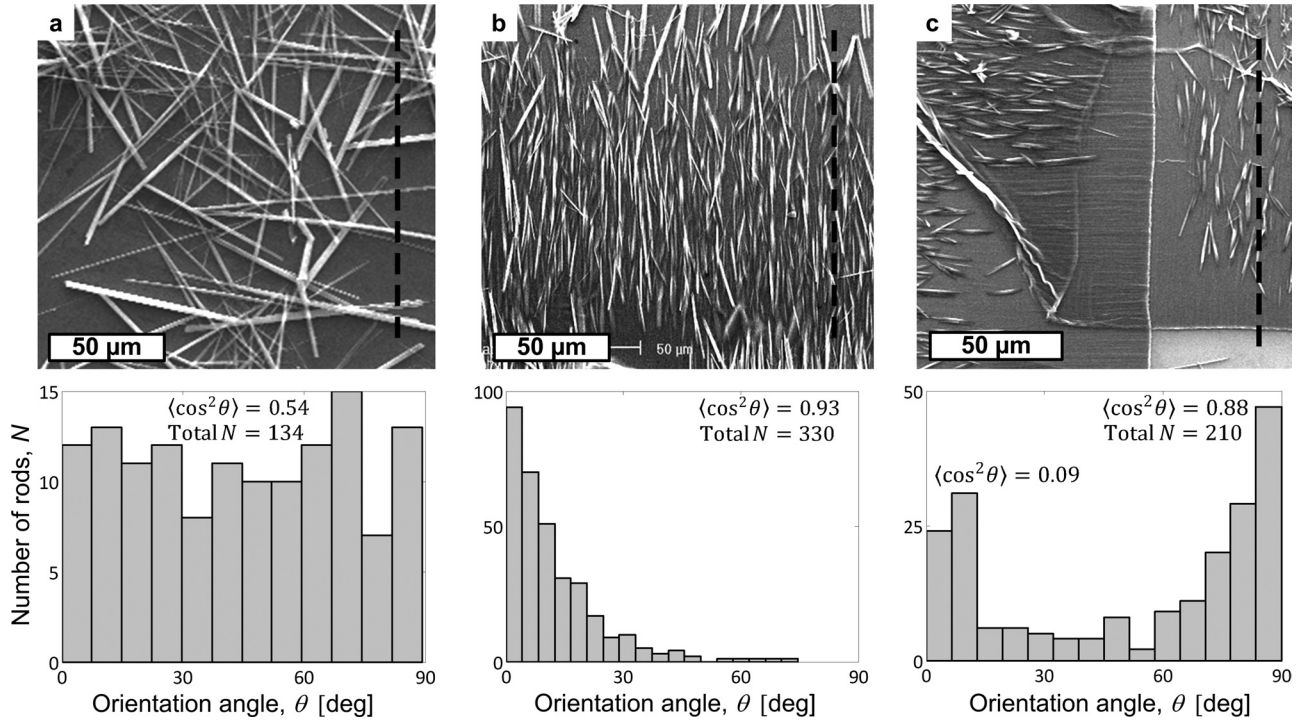

Figure 2. Scanning electron microscopy (SEM) images after synthesis of C_{60} rods on bare silicon (a), unidirectional CNT film (b), and bidirectional CNT film (c). Accompanying histograms are below each SEM, showing distribution of rod orientation relative to axis indicated by black dashed lines.

$\langle \cos^2 \theta \rangle$, where θ is the orientation angle of each rod relative to a reference axis (dashed line). This parameter has been used to quantify the order of other anisotropic structures including polymer chains,[21] liquid crystals,[22] and CNTs.[23] Note that $\langle \cos^2 \theta \rangle = 1$ corresponds to perfect parallel alignment of the rods with the CNTs, while $\langle \cos^2 \theta \rangle = 1/2$ represents random order. The C_{60} rods are randomly oriented when crystallized on bare silicon (Figure 2a; $\langle \cos^2 \theta \rangle = 0.54$), while those crystallized on CNTs are strongly correlated to the direction of CNT alignment (Figure 2b, 2c; $\langle \cos^2 \theta \rangle > 0.8$). On bare silicon, we occasionally observe areas where the solvent droplet becomes pinned to the substrate during evaporation. This causes a locally higher density of rods to form in arrangements that resemble drying rings, as in the "coffee stain" phenomenon (see the Supporting Information, Figure S1).[24] At these locations, the pinned meniscus does slightly influence local rod orientation, resulting in $\langle \cos^2 \theta \rangle < 0.7$. This likely occurs due to capillary forces that orient the rods as well as fluid flow and solute concentration gradients near the meniscus,[24,25] Thus, pinning of the meniscus on a flat substrate is not as uniformly effective in aligning the rods as compared to the CNT templates, albeit by a different mechanism.

Further investigation by electron microscopy shows that the C_{60} rods penetrate beneath the surface of the CNT films, and that CNTs pierce through the C_{60} crystals. A magnified view of the hierarchical, aligned morphology of the CNTs and CNT bundles is shown in **Figure 3**a–b. The existence of rods both on top and beneath the CNTs (Figure 3c) suggests that C_{60} rods can nucleate and grow on the surface of the CNT film and/or within the film. In both cases the rod growth direction is influenced by the CNTs. As seen here and in Figure 3d, the CNT are laced through the C_{60} rods, forming a true hybrid material, where up to $\approx 10^3$ CNTs may be incorporated into a single crystal (≈1 μm width), based on the packing density of the CNT film. Transmission electron microscopy (TEM) confirms that individual CNTs are connected to the side facet of the C_{60} rod (Figure 3e) and that the crystal structure of the rod is not disrupted by the CNTs (Figure 3f), which we later substantiate by X-ray diffraction.

Characteristic Raman spectroscopy peaks of C_{60} and CNTs allow for their identification within the hybrid film. We profile a single C_{60} rod that is partially embedded in the CNT film, and has one end exposed (**Figure 4**a) with a focused beam of less than 1 μm at the sample. Initially at (1), where the C_{60} rod is fully exposed, the characteristic C_{60} peak at ≈1468 cm^{-1}[26] is strong and discernable in the presence of the weaker CNT peaks near 1350 cm^{-1} and 1580 cm^{-1} (D- and G-bands, respecitvely).[27] The intensity of the C_{60} peak declines relative to the CNT G-band as the beam is scanned along the length of the rod [(2),(3)], matching with the transition of the rod into the CNT film. The peak position does not shift in frequency over the length of the rod, indicating that no chemical modification of the C_{60} molecules takes place before or during crystallization (e.g., via polymerization[28]). No spectroscopic features of the C_{60} are observed away from the rod at (4), confirming that the synthesis process leaves C_{60} highly localized around the crystals.

We determine the crystal structure of the C_{60} rods by grazing incidence X-ray diffraction (GIXD) measurements (Figure 4b) using synchrotron radiation and a 2D area detector. These

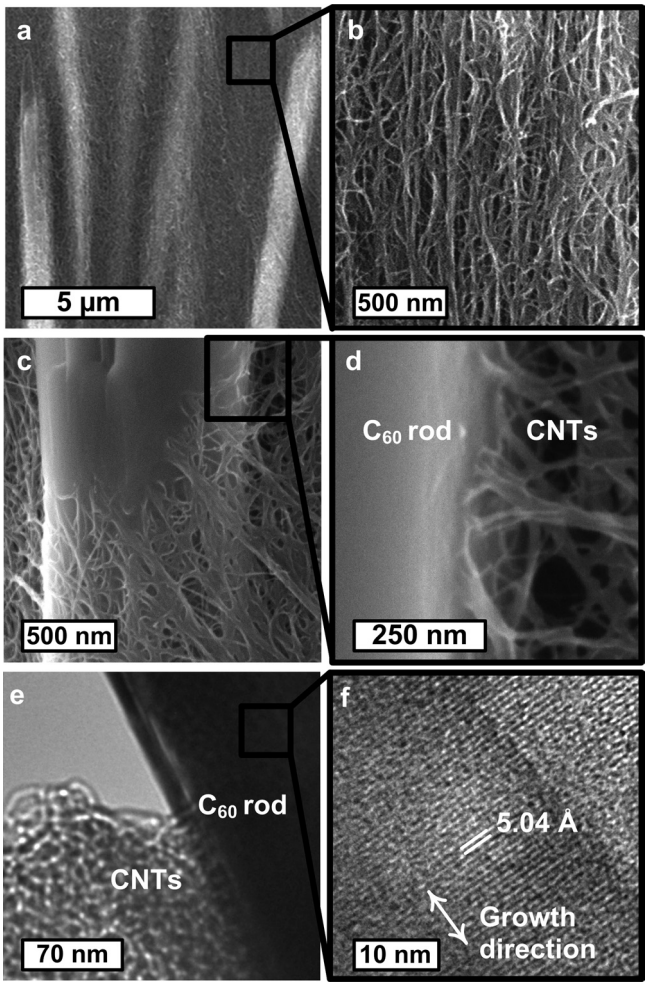

Figure 3. High-resolution electron microscopy of C_{60}-CNT hybrid material. a) SEM image of C_{60} rods aligned to the CNTs; b) Higher magnification of area between C_{60} crystals, showing aligned CNTs and CNT bundles; c) a single C_{60} rod that pierces through the CNT film, showing a smooth transition between CNTs and the C_{60} crystal and interconnection with further magnification in (d). CNT bundles are penetrating the side of the C_{60} rod. e) TEM image of the interface between CNTs and C_{60} crystal with higher magnification in (f).

measurements show the as-received C_{60} powder has a face-centered cubic (FCC) crystal structure with the lattice parameter $a = 14.3$ Å,[4,29] whereas the C_{60} rods grown on bare silicon and on CNT films both have a hexagonal structure ($a = 23.4$ Å, $c = 10.3$ Å), which is consistent with previous studies of C_{60} synthesized from *m*-xylene.[1,4,30] This change in packing from the higher-density FCC phase is due to the incorporation of trace solvent molecules at interstices,[4,6,30,31] where the C_{60}:*m*-xylene composition is 3:2.[30] Solvent is incoporated with the crystal partially due to the strong association between the its aromatic structure and the electron-rich hexagonal faces of C_{60},[32] as well as kinetics of the crystallization process, both of which are discussed later. A large difference in the scattered X-ray intensity is observed when the beam is aligned parallel versus perpendicular to the CNTs, emphasizing the crystallographic anisotropy of the hybrid material. C_{60} rods synthesized from *m*-xylene are known to crystallize

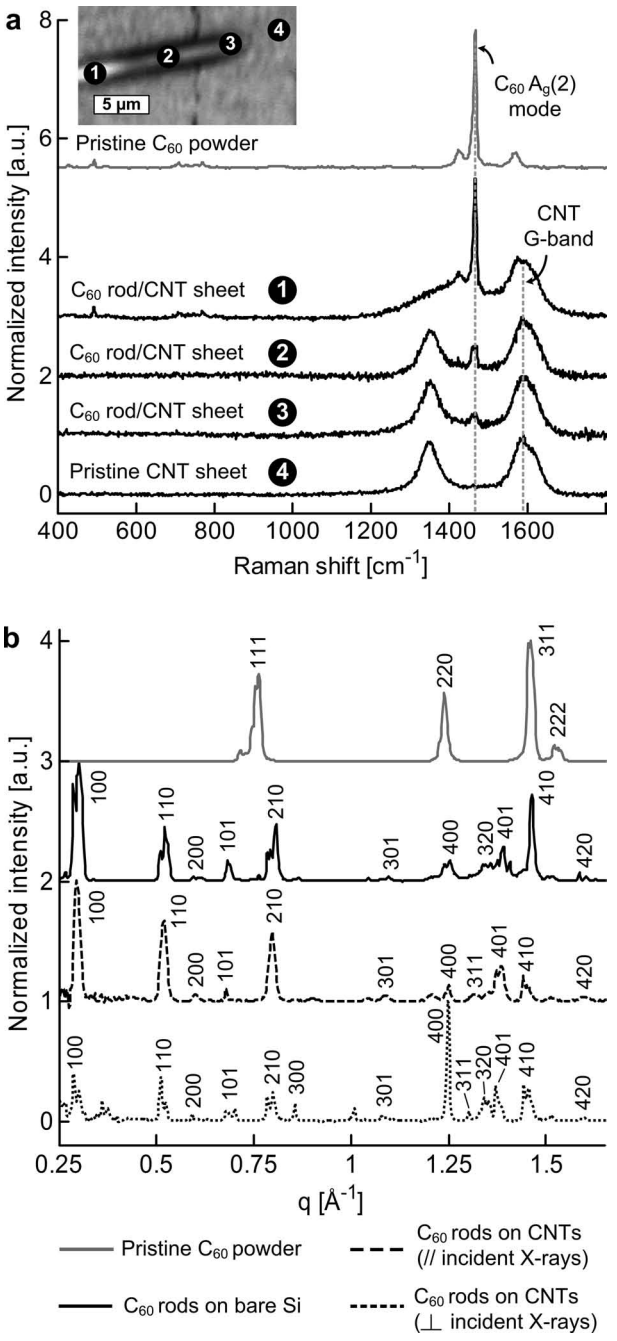

Figure 4. Structural characterization of a C_{60}-CNT hybrid film. a) Micro-Raman spectroscopy (λ = 514 nm) profile of a C_{60} rod that is partially embedded in a CNT film is compared to a spectrum taken from as-received C_{60} powder. The ratio of $I_G/I_D \approx 1.2$ observed here is typical for multi-wall CNTs synthesized by our thermal CVD process. b) GIXD data showing scattering intensity as a function of scattering vector q (where $q = 4\pi/\lambda \sin\psi$, and ψ is the scattering angle). The C_{60} crystals synthesized on CNTs are indexed as hexagonal lattice (a = 22.4 Å, c = 10.3 Å). See Figure S2 in the Supporting Information for an example of a 2D scattering image and further analysis.

along the *c*-axis (001),[3,6] and the crystal lattice spacing we measure from TEM (5.04 Å) in Figure 3f is approximately half of *c* because there are two crystal planes per unit cell.

4. Enhanced Kinetics of C_{60} Crystallization

Although the presence of CNTs does not alter the structure of the C_{60} crystals, C_{60} crystal growth on CNT films is significantly faster than on bare silicon. We use in situ optical microscopy to measure rod length versus time, as shown in **Figure 5**. The lengthening kinetics of C_{60} rods on CNTs are 8.6 times faster than on bare silicon (average rates ≈1.8 and 0.2 μm sec^{-1}, respectively), and growth terminates when the solvent fully evaporates from the substrate. After this occurs, the average length of the crystals is nearly identical on both substrates (16.1 and 15.5 μm, respectively), yet the standard deviation of length is smaller on CNTs (1.8 and 4.1 μm, respectively). The average width of the C_{60} rods in both cases is 1.3 ± 0.4 μm when growth terminates. The length distribution broadens with time on Si, yet narrows with time on CNTs, suggesting that the CNT substrate also enables a more uniform delivery of C_{60} to the growth sites. We also note that the rods do not move or rotate during observable stages of growth on CNT films, yet they remain straight and predominantly follow the CNT direction as growth proceeds. By guiding the delivery of the C_{60} dispersion by motion of a razor blade at constant velocity and distance from the film, we verify that the direction of crystallization is determined by the CNTs and not by the direction of liquid infiltration. Indeed, while directed meniscus motion controls the alignment of C_{60} rods on bare silicon, the rods always align to the CNTs even when the solvent is drawn over the CNTs in the perpendicular direction (see the Supporting Information, Figure S3).

Additional control experiments reinforce that both the physical and chemical characteristics of CNTs influence the rapid, directed crystallization of C_{60} (data not shown). First, we observe a very low density of rods on highly ordered pyrolytic graphite (HOPG), which presents similar chemical compatibility to C_{60} as CNTs. This is due to the smooth surface of HOPG and the strong wetting of *m*-xylene on HOPG, which accelerate evaporation and inhibit prolonged crystal growth. Therefore, the topography of the CNT film is important for a high nucleation density. Second, to preserve the physical texture and porosity of the CNT film while changing the surface chemistry, we conformally coated CNTs with alumina by atomic-layer deposition (ALD). On alumina-coated CNT films, rods form at low densities and are not aligned with the CNTs. This demonstrates that both the native surface chemistry and texture of the aligned CNT films are needed for directional crystallization. Third, instead of crystallizing C_{60} directly on CNTs, we alternatively prepared C_{60} rods in solution by liquid–liquid interface precipitation (LLIP)[33] and then drop-cast these rods onto CNT films. Even though the CNTs influence the motion of the meniscus during evaporation, the rods made by LLIP are not oriented with the same fidelity as those crystallized directly on the CNT films ($\langle\cos^2\theta\rangle = 0.72$ versus 0.93), and they do not penetrate into the CNT film. Therefore, in situ crystallization on CNT templates is necessary to direct the rod orientation. This finding also emphasizes how the present work is different than previous approaches to align pre-made nanostructures by directional wetting.[25,34]

We interpret these findings based on the anisotropic morphology of the CNT films as well as the physical interactions

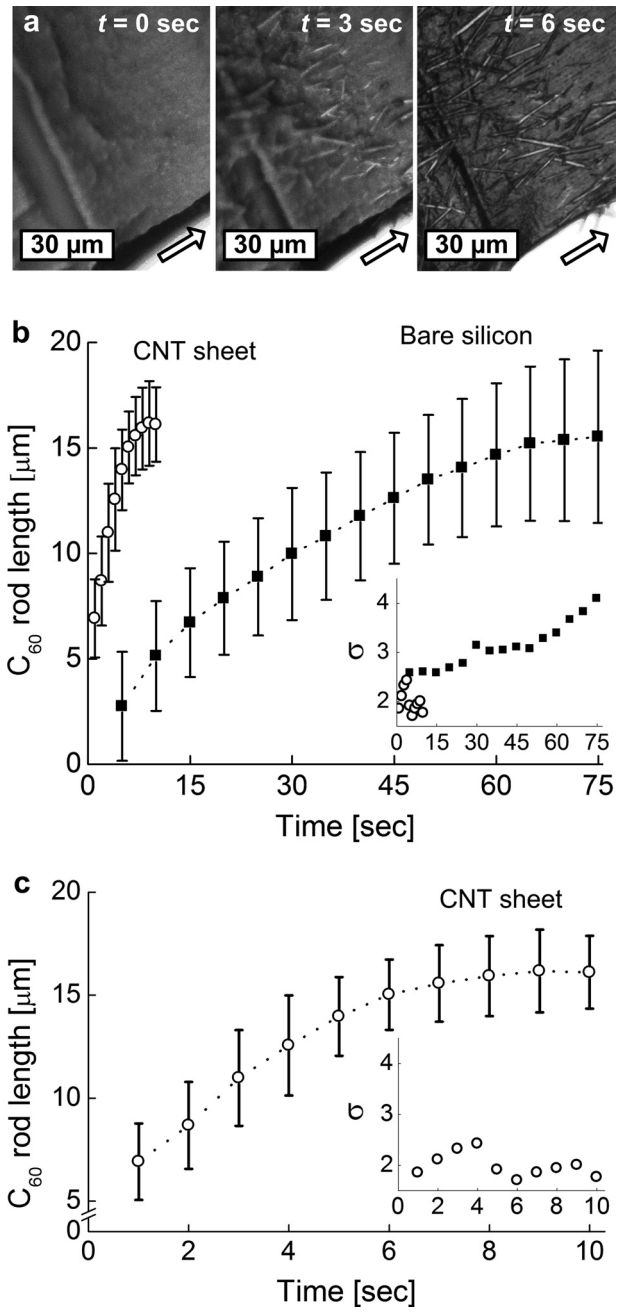

Figure 5. Lengthening kinetics of C_{60} rods on CNTs and silicon. a) Snapshots of real-time recording of the C_{60} crystal growth on a CNT film. b) Measurements of rod length versus time, comparing growth on CNTs (open circles) and on Si (filled squares), with the length versus time curve for growth on CNTs replicated in (c) with a rescaled *x*-axis to show similarity in shape and emphasize the difference in timescales. Each point and error bar represent the mean and standard deviation, respectively, for measurements taken from ten rods, while the inset plots show the standard deviation alone versus time for each case. $t = 0$ corresponds to the time at which a rod is first observed.

and known compatibility of CNTs, C_{60}, and the solvent. The CNT film is porous and is strongly wet by *m*-xylene; therefore, the solvent rapidly infiltrates the film upon drop-casting. Although the CNT packing fraction increases by as much as a factor of two during evaporation of the solvent,[19] the solvent and C_{60} clusters can still penetrate the CNT film because the size of the C_{60} clusters in solution (14.1 ± 2.9 nm, measured by dynamic light scattering, Figure S4) is less than the mean CNT–CNT nearest-neighbor spacing (i.e., pore size), which is approximately 20 nm for a packing fraction of 0.2. Also, the carbon atoms in both CNTs and C_{60} are sp^2-hybridized, although they differ in aromaticity due to the presence of pentagonal faces in addition to hexagonal ones in C_{60}. Calculations show that the binding energy between a single C_{60} molecule and the outer wall of a CNT (0.537 eV)[35] exceeds that for either C_{60}–C_{60} (0.277 eV)[36] or solvent–CNT interactions (0.232 eV);[37] therefore, C_{60} in solution should be strongly attracted to the surface of CNTs.

Precedence in literature indicates that nanoscale roughness and porosity promote nucleation of C_{60} crystals[38] as well as other materials.[15,39] Thus, favorable crystallization of C_{60} on CNTs is a specific case of a more general behavior, whereby nanostructured templates can assist crystallization via both fluidic and surface effects. Because of the strong C_{60}–CNT interaction, we hypothesize that rods nucleate when C_{60} clusters adhere to the CNTs while in solution, and then the crystal continues grows along CNTs by precipitation of the solute in a similar templating fashion previously observed in crystallization of polymers on CNTs.[40] This may be aided by adsorption and migration of C_{60} clusters along the CNTs, and the strong capillary action within the CNT film.[41] Surface defects are well known to act as favorable nucleation sites by restricting the mobility of adsorbed precursors, such as in vapor–solid growth of nanowires,[42] including formation of oxide nanostructures on CNT forests.[43] Thus, we expect the defect density of CNTs influences C_{60} crystal nucleation, and experiments with CNTs of different diameters (i.e., single-walled CNTs, which can have fewer defects) will be insightful. Likewise, the micro- and nanometer-scale surface texture of the CNT film (determined by the waviness and bundling of the CNTs) and the pore size (CNT spacing) within the film depend on the diameters and packing configuration of the CNTs, so controlling these characteristics may be a route to achieve enhanced control of selective crystal growth. For instance, previous studies found that bundles of CNTs selectively aid crystallization of organic molecules,[13] which Pan, et al. suggest is due at least in part to favorable adsorption sites created by interstitial pores between CNT bundles.[44]

5. Device Integration and Photocurrent Measurements

Finally, we electrically integrate CNT films as two-terminal devices to characterize the photoresponse of our material in the UV range. Our fabrication method (Figure 1) is scalable because it employs standard photolithography of TiN electrodes that are compatibile with high-temperature CVD of CNTs, and because capillary folding and drop-casting of C_{60} are straightforward solvent processes. **Figure 6**a demonstrates that the photocurrent of the hybrid C_{60}–CNT device is substantially greater than either CNTs alone or C_{60} rods alone. The linear *I*–*V* characteristics indicate that the hybrid device is a photoconductor,

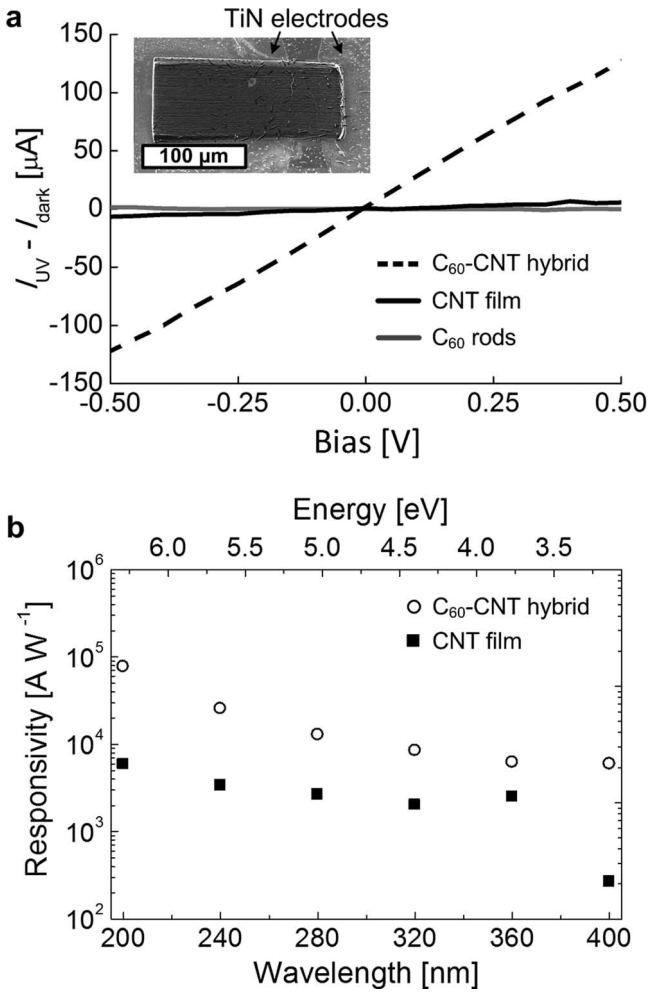

Figure 6. Photoresponse of CNT/C_{60} hybrid film devices. a) Photocurrent measurement (applied bias ± 0.5 V) of device as shown in the inset SEM, where photocurrent is defined as the change in current measured with UV illumination on and off. b) Responsivity (photocurrent divided by incident power) for range of UV wavelengths showing enhancement due to the addition of C_{60} to the CNT film. Each point represents the mean value taken from at least three measurements of the same device.

and for instance, the resistance at 400 nm decreases by more than 20 times after integrating C_{60} rods with the CNT device. The responsivity of the hybrid device is 10^3–10^5 A W^{-1} in the range of 400–200 nm irradiation (Figure 6b), respectively. This exceeds recent benchmarks for nanostructured photodetectors (e.g., ZnO or PbS quantum dots),[45] while our bias remains relatively low (0.5 V). Although the CNT device has an appreciable responsivity in this wavelength range (likely due to heat-induced changes in resistivity reslting from absorption of light[46]), the addition of C_{60} enhances the responsivity by approximately an order of magnitude.

The high photoconductivity of the hybrid film is the result of the interplay between the electronic structures of C_{60} and CNTs, as well as their hiearchical organization. We expect C_{60} crystals to generate excitons when illuminated by light with energy greater than the band gap of soild C_{60}, which is about 2.3 eV (540 nm).[47] Others have shown that individual C_{60} crystals with[48] or without[5] interstitial solvent molecules can generate photocurrent. The hierachical structure of our hybrid film allows charge carriers to be injected into the mulit-walled CNTs, which are metallic, and charge separation is also aided by the strong tendency of C_{60} to accept electrons.[7,8] Thus, holes are likely the injected charge carrier, and can pass through the circuit many times under the influence of the applied electric field (bias) before recombining with trapped electrons. While the absorption properties of C_{60}/*m*-xylene crystals in the tested wavelength range is relatively constant,[49] multi-walled CNTs show inceased absorption toward 200 nm,[50] which explains the upward trend in responsivity we observe in both the CNT and C_{60}–CNT devices. The large surface-area-to-volume ratio of the hybrid films also plays a role in the large responsivity, increasing absorption and increasing the abundance of surfaces and interfaces, which can trap charge carriers, delay recombination, and thus increase the responsivity of the device.[45,51] Recent studies have also demonstrated the advantages of combining C_{60} with CNTs in various devices to enhance the performance of photodetectors[8] and photovoltaics.[52] While some of these examples also incorporate other materials, such as effective electron donors, the addition of C_{60} to these complexes is key, and our CNT template technology could be combined with these previously studied matierials to achieve new device architectures.

6. Conclusions

We show that CNT films promote rapid crystallization of C_{60} from solution, and we harness the strong influence of the CNT direction to create multidirectional films. The C_{60} crystals are interconnected by CNTs, and the CNTs provide a conducting pathway to the C_{60} crystals, making a unique hybrid material, which shows utility and promise as an organic UV photodector with high responsivity. We assert that our methods and findings have general importance to the science and applications of crystal growth of other materials, including aromatic hydrocarbons, synthetic polymers, and biomolecules. In the future, more complex multi-directional CNT architectures[53] may find use as scaffolds for spatially programmable 3D self-assembly, where the formation and organization of crystals is predetermined by the nanoscale texture of the CNTs and their microscale form factor.

7. Experimental Section

Fabrication of C_{60}-CNT Hybrid Films: CNT growth was performed using both a horizontal quartz tube furnace (Thermo-Fisher Mini-Mite, 22 mm inner diameter, 12 inch heated length). The catalyst substrate which comprises a 10 nm Al_2O_3 underlayer and 1 nm Fe is deposited on (100) silicon wafers using e-beam evaporation, and patterned by lithography and lift-off.[16] For lithography, we used a SPR 220-3.0 photoresist. The lift-off was done by sonication in acetone followed by rinsing in isopropanol and evaporation using dry N_2. After installing the substrate and purging the reactor, the substrate was heated to the growth temperature in flowing H_2/He (100/400 sccm), and then C_2H_4 (100 sccm) was added for the growth duration. To prepare the laterally oriented (LO) CNTs, vertically aligned CNTs are grown from parallel catalyst lines with 20 µm width and 200 µm spacing. The CNT line patterns are then mechanically rolled using a 300 µm diameter stainless steel roller in a

custom-built force-controlled rolling machine.[19] To prepare radially oriented (RO) CNTs, acetone vapor is generated by boiling acetone in a flask and condensing the vapor onto vertically aligned CNT patterns (rings as shown in Figure 1). The capillary forces exerted by the acetone during condensation from the CNTs mechanically fold the CNTs into RO CNT films.[53] Optionally, atomic layer deposition (ALD) of Al_2O_3 is done in an Oxford ALD system with trimethylaluminum (TMA) and water as precursors. A deposition temperature of 200 °C for 100 cycles results in ≈10 nm of conformal coating of Al_2O_3 on the CNTs.

The C_{60} dispersion was prepared using *m*-xylene and C_{60} powder (99.5% purity; MTR, Ltd.) with a concentration of 1 mg mL^{-1}, which is below the solubility limit of C_{60} in *m*-xylene. The mixture was sonicated for 30 min immediately after the addition of the powder to the solvent. Droplets (<10 μL) of C_{60} dispersion were placed on the substrates using a micropipette. The solvent was allowed to completely evaporate from the substrate under ambient conditions. Real-time videos were recorded with a 3.1 megapixel CMOS color camera (Lumenera Infinity 1-3C) at 15 frames per second, and snapshots at specified time intervals were selected for processing and measurements.

Materials Characterization: A Malvern Zetasizer Nanoseries was used to perform dynamic light scattering for estimation of the C_{60} cluster size in *m*-xylene. SEM was performed using a Philips XL30-FEG and a FEI Nova Nanolab, and TEM was performed on a JEOL 3011 HREM. Micro-Raman spectroscopy was performed using a Renishaw inVia Raman microscope equipped with a Leica microscope, RenCam CCD detector, 514 nm He–Ne laser. The spot size was <1 μm. In Figure 4a, peaks in the C_{60} powder spectrum at approximately 470 cm^{-1} and 1468 cm^{-1} represent the radial breathing and pentagonal-pinch vibrational modes of C_{60}, respectively.[26] Characteristic peaks of multi-wall CNTs appear near 1350 cm^{-1} and 1580 cm^{-1},[27] corresponding to the D- and G-bands, respectively.

Grazing incidence X-ray diffraction (GIXD) measurements were performed at the Stanford Synchrotron Radiation Lightsource (SSRL) using beamline 11–3 with a photon wavelength of 0.09758 nm. The scattering intensity was detected on a 2D image plate (MAR-345) with a pixel size of 150 μm (2300 pixel × 2300 pixel) and analyzed using the software package WxDiff, provided by Dr. Stefan Mannsfeld. The detector was located at a distance of 400.9 mm from the sample center. The incidence angle was chosen in the range of 0.10°–0.12° to optimize the signal to-background ratio. The beam size was 50 μm × 150 μm, which resulted in a beam footprint on sample 150 μm wide over the entire length of the 5–10 mm long sample. The data were distortion-corrected (θ-dependent image distortion introduced by planar detector surface) before performing quantitative analysis on the images. The overall resolution in the GIXD experiments, dominated by the sample size, was about 0.08 $Å^{-1}$.

The samples are loaded into a probe station measuring the *I–V* characteristics of the material as it was illuminated at wavelengths ranging from 200 to 400 nm using a Sutter Instruments Co. Lambda 10-2 source. We measure the difference in current in dark conditions and during UV exposure for C_{60} rods, CNT sheets and the C_{60}-CNT hybrids with an applied bias of ± 0.5V at an illumination power range of 8.4–131 μW cm^{-2} for 200–400 nm, respectively. Normalizing the change in current (I_{UV}–I_{dark}/I_{dark}) shows an increase in current of 5% in the case C_{60}–CNT hybrids, while this is more than 10 fold of pure CNT sheets or pure C_{60} in our setup.

Supporting Information

Supporting Information is available from the Wiley Online Library or from the author.

Acknowledgements

Financial support was provided by the National Science Foundation Nanomanufacturing Program (CMMI-0927634), for CNT fabrication; and the Office of Naval Research (N000141010556), for material characterization at Michigan and for manuscript preparation. Electron microscopy was performed at the University of Michigan Electron Microbeam Analysis Library (EMAL), which is supported by NSF (DMR-0315633). K. Patel was supported in part by the Summer Undergraduate Research Experience (SURE) program at the University of Michigan. E. Verploegen was supported by the Kodak Fellows Program at Stanford University. M. De Volder was supported by the fund for Belgian Fund for Scientific Research - Flanders (FWO). We thank Kai Sun for assistance with TEM imaging. X-ray diffraction was carried out at the Stanford Synchrotron Radiation Lightsource, which is a Directorate of SLAC National Accelerator Laboratory, and an Office of Science User Facility operated by Stanford University for the U.S. Department of Energy Office of Science. We also thank Saikat Roy for assistance with Raman spectroscopy using the facilities of Adam Matzger at Michigan, Christine Andres for assistance with DLS measurements using the facilities of Nicholas Kotov at Michigan, and Kiki Minoglou for assistance with UV measurements at IMEC.

Received: October 6, 2011
Published online: November 29, 2011

[1] C. Park, H. J. Song, H. C. Choi, *Chem. Commun.* **2009**, 4803–4805.
[2] a) H. Y. Gan, H. B. Liu, Y. L. Li, L. B. Gan, L. Jiang, T. G. Jiu, N. Wang, X. R. He, D. B. Zhu, *Carbon* **2005**, *43*, 205–208; b) K. Miyazawa, J. Minato, T. Yoshii, M. Fujino, T. Suga, *J. Mater. Res.* **2005**, *20*, 688–695; c) J. Minato, K. Miyazawa, *Carbon* **2005**, *43*, 2837–2841; M. Sathish, K. Miyazawa, *J. Am. Chem. Soc.* **2007**, *129*, 13816–13817.
[3] H. X. Ji, J. S. Hu, L. J. Wan, Q. X. Tang, W. P. Hu, *J. Mater. Chem.* **2008**, *18*, 328–332.
[4] L. Wang, B. B. Liu, D. Liu, M. G. Yao, Y. Y. Hou, S. D. Yu, T. Cui, D. M. Li, G. T. Zou, A. Iwasiewicz, B. Sundqvist, *Adv. Mater.* **2006**, *18*, 1883.
[5] H. S. Shin, S. M. Yoon, Q. Tang, B. Chon, T. Joo, H. C. Choi, *Angew. Chem. Int. Ed.* **2008**, *47*, 693–696.
[6] M. G. Yao, B. M. Andersson, P. Stenmark, B. Sundqvist, B. B. Liu, T. Wagberg, *Carbon* **2009**, *47*, 1181–1188.
[7] S. Saito, A. Oshiyama, *Phys. Rev. Lett.* **1991**, *66*, 2637–2640.
[8] M. S. Arnold, J. D. Zimmerman, C. K. Renshaw, X. Xu, R. R. Lunt, C. M. Austin, S. R. Forrest, *Nano Lett.* **2009**, *9*, 3354–3358.
[9] K. Esfarjani, M. Zebarjadi, Y. Kawazoe, *Phys. Rev. B* **2006**, *73*, 085406.
[10] L. Ma, J. Ouyang, Y. Yang, *Appl. Phys. Lett.* **2004**, *84*, 4786–4788.
[11] a) T. Doi, K. Koyama, Y. Chiba, H. Tsuji, K. Ueno, S.-R. Chen, N. Aoki, J. P. Bird, Y. Ochiai, *Jpn. J. Appl. Phys.* **2010**, *49*, 04DN12; b) T. D. Anthopoulos, B. Singh, N. Marjanovic, N. S. Sariciftci, A. M. Ramil, H. Sitter, M. Colle, D. M. de Leeuw, *Appl. Phys. Lett.* **2006**, *89*, 213504–213503.
[12] Y. Z. Jin, R. J. Curry, J. Sloan, R. A. Hatton, L. C. Chong, N. Blanchard, V. Stolojan, H. W. Kroto, S. R. P. Silva, *J. Mater. Chem.* **2006**, *16*, 3715–3720.
[13] S. Liu, A. L. Briseno, S. C. B. Mannsfeld, W. You, J. Locklin, H. W. Lee, Y. Xia, Z. Bao, *Adv. Funct. Mater.* **2007**, *17*, 2891–2896.
[14] N. E. Chayen, *Curr. Opin. Struct. Biol.* **2004**, *14*, 577–583.
[15] a) J. A. van Meel, R. P. Sear, D. Frenkel, *Phys. Rev. Lett.* **2010**, *105*, 205501; b) E. Curcio, V. Curcio, G. D. Profio, E. Fontananova, E. Drioli, *J. Phys. Chem. B* **2010**, *114*, 13650–13655; c) N. E. Chayen, E. Saridakis, R. P. Sear, *Proc. Natl. Acad. Sci. USA* **2006**, *103*, 597–601.
[16] A. Hart, A. Slocum, *J. Phys. Chem. B* **2006**, *110*, 8250–8257.
[17] a) K. Hata, D. N. Futaba, K. Mizuno, T. Namai, M. Yumura, S. Iijima, *Science* **2004**, *306*, 1362–1364; b) M. F. L. De Volder, D. O. Vidaud, E. R. Meshot, S. Tawfick, A. J. Hart, *Microelectron. Eng.* **2010**, *87*, 1233–1238.

[18] M. Bedewy, E. Meshot, H. Guo, E. Verploegen, W. Lu, A. Hart, *J. Phys. Chem. C* **2009**, *113*, 20576–20582.
[19] S. Tawfick, K. O'Brien, A. Hart, *Small* **2009**, *5*, 2467–2473.
[20] a) S. Tawfick, M. De Volder, A. J. Hart, *Langmuir* **2011**, *27*, 6389–6394; b) M. De Volder, S. H. Tawfick, S. J. Park, D. Copic, Z. Z. Zhao, W. Lu, A. J. Hart, *Adv. Mater.* **2010**, *22*, 4384–4389 ; c) Z. Z. Zhao, S. H. Tawfick, S. J. Park, M. De Volder, A. J. Hart, W. Lu, *Phys. Rev. E* **2010**, *82*, 41605; d) M. F. L. De Volder, S. Tawfick, S. J. Park, A. J. Hart, *ACS Nano* **2011**, *5*, 7310–7317.
[21] P. H. Hermans, *Contribution to the physics of cellulose fibres; a study in sorption, density, refractive power and orientation*, Elsevier Pub. Co., Amsterdam **1946**.
[22] S. Ghosh, *Il Nuovo Cimento D* **1984**, *4*, 229–244.
[23] B. Wang, R. Bennett, E. Verploegen, A. Hart, R. Cohen, *J. Phys. Chem. C* **2007**, *111*, 5859–5865.
[24] R. D. Deegan, O. Bakajin, T. F. Dupont, G. Huber, S. R. Nagel, T. A. Witten, *Nature* **1997**, *389*, 827–829.
[25] R. Sharma, C. Y. Lee, J. H. Choi, K. Chen, M. S. Strano, *Nano Lett.* **2007**, *7*, 2693–2700.
[26] D. S. Bethune, G. Meijer, W. C. Tang, H. J. Rosen, W. G. Golden, H. Seki, C. A. Brown, M. S. Devries, *Chem. Phys. Lett.* **1991**, *179*, 181–186.
[27] M. S. Dresselhaus, G. Dresselhaus, R. Saito, A. Jorio, *Phys. Rep.* **2005**, *409*, 47–99.
[28] A. M. Rao, P. Zhou, K. A. Wang, G. T. Hager, J. M. Holden, Y. Wang, W. T. Lee, X. X. Bi, P. C. Eklund, D. S. Cornett, M. A. Duncan, I. J. Amster, *Science* **1993**, *259*, 955–957.
[29] Y. J. Guo, N. Karasawa, W. A. Goddard, *Nature* **1991**, *351*, 464–467.
[30] M. V. Korobov, E. B. Stukalin, A. L. Mirakyan, I. S. Neretin, Y. L. Slovokhotov, A. V. Dzyabchenko, A. I. Ancharov, B. P. Tolochko, *Carbon* **2003**, *41*, 2743–2755.
[31] a) E. V. Skokan, V. I. Privalov, I. V. Arkhangel'skii, V. Y. Davydov, N. B. Tamm, *J. Phys. Chem. B* **1999**, *103*, 2050–2053; b) A. Masuhara, Z. Q. Tan, H. Kasai, H. Nakanishi, H. Oikawa, *Jan. J. Appl. Phys.* **2009**, *48*, 3.
[32] R. G. Alargova, S. Deguchi, K. Tsujii, *J. Am. Chem. Soc.* **2001**, *123*, 10460–10467.
[33] a) H. X. Ji, J. S. Hu, Q. X. Tang, W. G. Song, C. R. Wang, W. P. Hu, L. J. Wan, S. T. Lee, *J. Phys. Chem. C* **2007**, *111*, 10498–10502; b) K. Miyazawa, Y. Kuwasaki, A. Obayashi, M. Kuwabara, *J. Mater. Res.* **2002**, *17*, 83–88.
[34] a) J. K. Lim, B. Y. Lee, M. L. Pedano, A. J. Senesi, J.-W. Jang, W. Shim, S. Hong, C. A. Mirkin, *Small* **2010**, *6*, 1736–1740; b) S. Liu, J. B. H. Tok, J. Locklin, Z. Bao, *Small* **2006**, *2*, 1448–1453.
[35] a) L. A. Girifalco, M. Hodak, R. S. Lee, *Phys. Rev. B* **2000**, *62*, 13104; b) R. S. Ruoff, A. P. Hickman, *J. Phys. Chem.* **1993**, *97*, 2494–2496.
[36] L. A. Girifalco, M. Hodak, *Phys. Rev. B* **2002**, *65*, 125404.
[37] L. M. Woods, S. C. Babrevedescu, T. L. Reinecke, *Phys. Rev. B* **2007**, *75*, 155415.
[38] A. L. Briseno, S. C. B. Mannsfeld, M. M. Ling, S. Liu, R. J. Tseng, C. Reese, M. E. Roberts, Y. Yang, F. Wudl, Z. Bao, *Nature* **2006**, *444*, 913–917.
[39] Y. Diao, T. Harada, A. S. Myerson, T. Alan Hatton, B. L. Trout, *Nat. Mater.* **2011**; Y. Diao, A. S. Myerson, T. A. Hatton, B. L. Trout, *Langmuir* **2011**, *27*, 5324–5334.
[40] a) C. Y. Li, L. Li, W. Cai, S. L. Kodjie, K. K. Tenneti, *Adv. Mater.* **2005**, *17*, 1198–1202; b) B. Li, L. Li, B. Wang, C. Y. Li, *Nat. Nanotechnol.* **2009**, *4*, 358–362.
[41] T. Sugimoto, *Adv. Colloid Interface Sci.* **1987**, *28*, 65–108.
[42] a) H. Heyer, *Angew. Chem. Int. Ed.* **1966**, *5*, 67–78; b) G. W. Sears, *Acta Metall.a* **1955**, *3*, 361–366; c) M. J. Bierman, Y. K. A. Lau, A. V. Kvit, A. L. Schmitt, S. Jin, *Science* **2008**, *320*, 1060–1063.
[43] a) J. G. Ok, S. H. Tawfick, K. A. Juggernauth, K. Sun, Y. Zhang, A. J. Hart, *Adv. Funct. Mater.* **2010**, *20*, 2470–2480; b) D. Eder, *Chem. Rev.* **2010**, *110*, 1348–1385.
[44] B. Pan, B. Xing, *Environ. Sci. Technol.* **2008**, *42*, 9005–9013.
[45] G. Konstantatos, E. H. Sargent, *Nat. Nanotechnol.* **2010**, *5*, 391–400.
[46] a) M. E. Itkis, F. Borondics, A. Yu, R. C. Haddon, *Science* **2006**, *312*, 413–416; b) G. Vera-Reveles, T. J. Simmons, M. Bravo-Sánchez, M. A. Vidal, H. Navarro-Contreras, F. J. González, *ACS Appl. Mater. Interfaces* **2011**, *3*, 3200–3204.
[47] R. W. Lof, M. A. Vanveenendaal, B. Koopmans, H. T. Jonkman, G. A. Sawatzky, *Phys. Rev. Lett.* **1992**, *68*, 3924–3927.
[48] Y. Zhang, W. Liu, L. Jiang, L. Z. Fan, C. R. Wang, W. P. Hu, H. Z. Zhong, Y. F. Li, S. H. Yang, *J. Mater. Chem.* **2010**, *20*, 953–956.
[49] L. Wang, B. B. Liu, S. D. Yu, M. G. Yao, D. D. Liu, Y. Y. Hou, T. Cui, G. T. Zou, B. Sundqvist, H. You, D. K. Zhang, D. G. Ma, *Chem. Mater.* **2006**, *18*, 4190–4194.
[50] S. Banerjee, S. S. Wong, *Nano Lett.* **2002**, *2*, 195–200.
[51] G. Konstantatos, L. Levina, A. Fischer, E. H. Sargent, *Nano Lett.* **2008**, *8*, 1446–1450; J. S. Liu, *Appl. Phys. Lett.* **2010**, *97*, 251102.
[52] a) D. J. Bindl, M.-Y. Wu, F. C. Prehn, M. S. Arnold, *Nano Lett.* **2010**, *11*, 455–460; b) V. C. Tung, J.-H. Huang, I. Tevis, F. Kim, J. Kim, C.-W. Chu, S. I. Stupp, J. Huang, *J. Am. Chem. Soc.* **2011**, *133*, 4940–4947; c) C. Li, Y. Chen, S. A. Ntim, S. Mitra, *Appl. Phys. Lett.* **2010**, *96*, 143303.
[53] M. De Volder, S. H. Tawfick, S. J. Park, D. Copic, Z. Zhao, W. Lu, A. J. Hart, *Adv. Mater.* **2010**, *22*, 4384–4389.